Supporting Information

Mass spectrometry imaging reveals a gradient of cancer-like metabolic states in the vicinity of cancer not seen in morphometric margins from microscopy

Michael Woolman[a,b], Lauren Katz[a,b], Georgia Gopinath[a,b], Taira Kiyota[c], Claudia M. Kuzan-Fischer[g,h], Isabelle Ferry[g,h], Mark Zaidi[b,i], Kaitlyn Peters[a,b], Ahmed Aman[c,j], Trevor McKee[a,i], Fred Fu[i], Siham Amara-Belgadi[b], Craig Daniels[g,h], Brad G. Wouters[a,b], James T. Rutka[d,g], Howard J. Ginsberg[a,d,e,f], Chris McIntosh[a,b,k] and Arash Zarrine-Afsar [a,b,d,e,*]

[a] Techna Institute for the Advancement of Technology for Health, University Health Network, 100 College Street, Toronto, ON, M5G 1P5, Canada
[b] Department of Medical Biophysics, University of Toronto, 101 College Street, Toronto, ON, M5G 1L7, Canada
[c] Drug Discovery Program, Ontario Institute for Cancer Research, 661 University Avenue, Toronto, ON M5G 0A3, Canada
[d] Department of Surgery, University of Toronto, 149 College Street, Toronto, ON, M5T 1P5, Canada
[e] Keenan Research Center for Biomedical Science & the Li Ka Shing Knowledge Institute, St. Michael's Hospital, 30 Bond Street, Toronto, ON, M5B 1W8, Canada
[f] Institute of Biomaterials and Biomedical Engineering, University of Toronto, 164 College Street, Toronto, ON, M5S 3G9, Canada
[g] Arthur and Sonia Labatt Brain Tumor Research Centre, The Hospital for Sick Children, Toronto, ON, M5G 1X8, Canada
[h] Developmental & Stem Cell Biology Program, The Hospital for Sick Children, 686 Bay Street, Toronto, ON, M5G 0A4, Canada
[i] STTARR Innovation Centre, 101 College Street, Toronto, ON, M5G 1L7, Canada
[j] Leslie Dan Faculty of Pharmacy, 144 College St, Toronto, ON, M5S 3M2, Canada
[k] Peter Munk Cardiac Centre, Joint Department of Medical Imaging, University Health Network, Toronto, ON, M5G-2N2, Canada & Vector Institute for Artificial Intelligence, Toronto, ON, M5G-1M1, Canada

*Corresponding author: Arash Zarrine-Afsar
Email:arash.zarrine.afsar@utoronto.ca
101 College Street, Room 7-207,
MaRS Building, Princess Margaret Cancer Research Tower, 7th floor (STTARR)
Toronto, ON M5G 1L7
TEL (Office): ++1-416-581-8473

Authorship:
Designed research: AZ-A, CM, AA, TK, MW, TMcK, FF, MZ
Performed research: MW, LK, GG, KP, TK, FF, MZ
Created and provided reagents for analysis: CMKF, IF
Analyzed results: AZ-A, CM, MW, LK, GG, TK, MZ, KP, SAB
Provided supervisory and support: AZ-A, CM, AA, BGW, HJG, JTR, TMcK
Wrote the manuscript: AZ-A, MW, LK, CD

Table of Contents

Target m/z (DESI-MS)	LC-MS (m/z)	RT (min)	Theoretical m/z	Error (ppm)	Ion form	Assignment	Predicted formula	Distinguishing fragments (ms/ms)
790.537	790.5403	10.3	790.5392	1.4	[M-H]-	PE(22:6/18:0) or PE(18:0/22:6)	$[C_{45}H_{77}NO_8P]$	m/z 79, m/z 97, m/z 122, m/z 140, m/z 153, m/z 283, m/z 327, m/z 462, m/z 480, m/z 506, m/z 524
941.812	941.7073	8.6	941.7087	-1.4	[M-H]-	MGDG(48:6)	$[C_{57}H_{97}O_{10}]$	Exact mass only
804.548	804.576	10.18	804.5755	0.6	[M+formate]-	PC(18:1/16:0) or PC(16:0/18:1)	$[C_{43}H_{83}NO_{10}P]$	m/z 79, m/z 97, m/z 153, m/z 168, m/z 224, m/z 255, m/z 281, m/z 462, m/z 480, m/z 488, m/z 506, m/z 744
834.53	834.5313	8.9	834.5291	2.6	[M-H]-	PS(22:6/18:0) or PS(18:0/22:6)	$[C_{46}H_{77}NO_{10}P]$	m/z 79, m/z 97, m/z 153, m/z 283, m/z 327, m/z 419, m/z 437, m/z 463, m/z 481, m/z 747
778.548	778.5594	10	778.5598	-0.5	[M+formate]-	PC(16:0/16:0)	$[C_{41}H_{81}NO_{10}P]$	m/z 79, m/z 97, m/z 153, m/z 168, m/z 224, m/z 255, m/z 462, m/z 480, m/z 718
888.625	888.6241	11.3	888.624	0.1	[M-H]-	SHexCer(d18:1/24:1) or SHexCer(d24:1/18:1)	$[C_{48}H_{90}NO_{11}S]$	m/z 97, m/z 139, m/z 241, m/z 257, m/z 300
854.519	854.6725	13.4	854.6727	-0.2	[M+formate]-	HexCer(d18:1/24:1)	$[C_{49}H_{92}NO_{10}]$	m/z 161, m/z 237, m/z 263, m/z 364, m/z 365, m/z 390, m/z 406, m/z 629, m/z 647, m/z 809

Table S1. Assignment of identity to healthy tissue ions that exhibit a gradient of cancer-like abundance in the vicinity of medulloblastoma cancer. HPLC-MS/MS was performed, as described in the methods section, on tissue extract material to determine the identity for each of the DESI-MS target ions shown in Fig. 1F to exhibit distance-dependent gradient behaviour in proximity of cancer. The accurate mass, retention time, theoretical mass and diagnostic fragments if applicable (observed), have been reported. This analysis was performed largely as described previously[1]. A variety of different classes of lipids, some of which are known to be synthesized from DHA are reported and assigned.

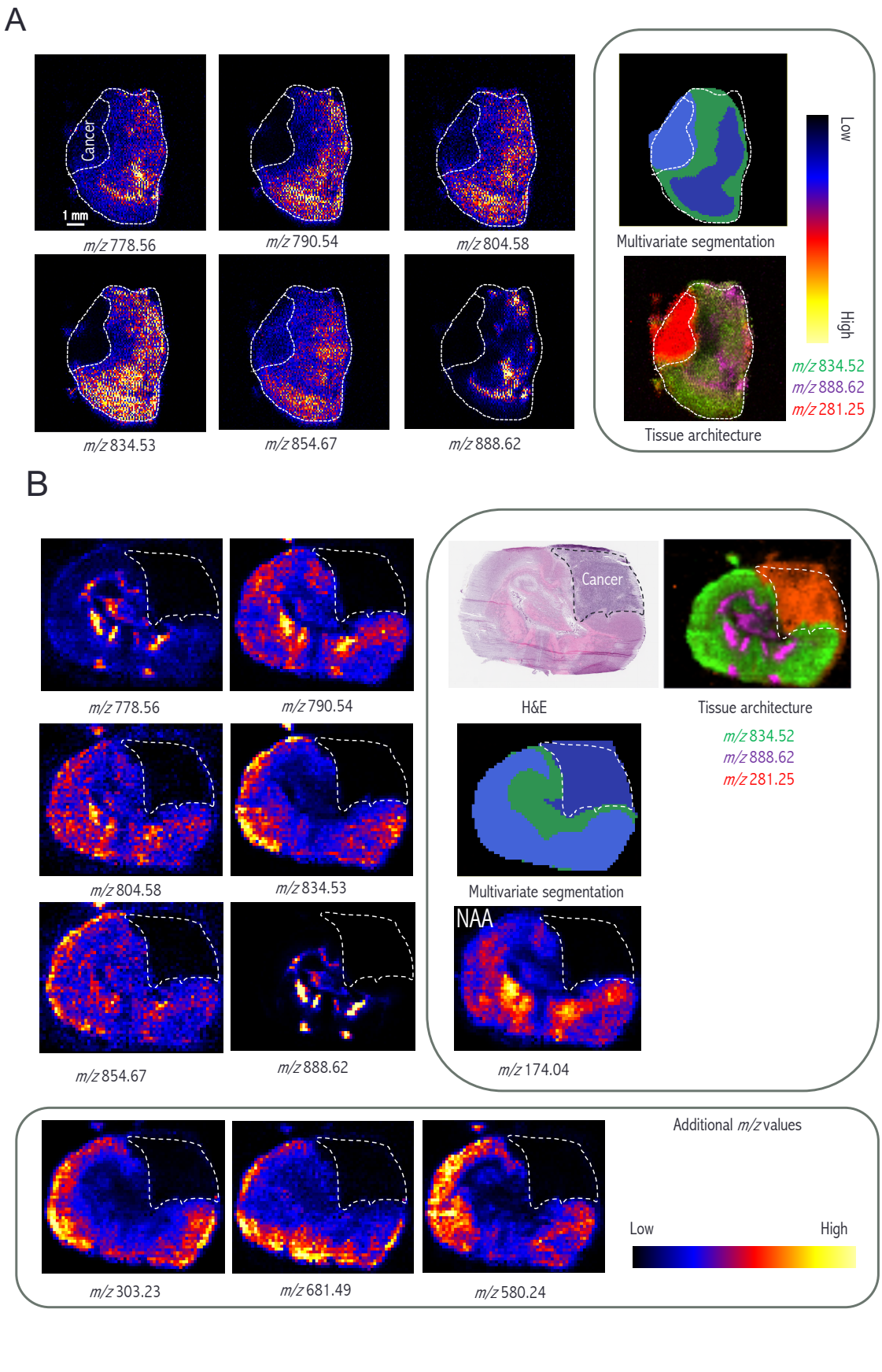
A
Cancer
1 mm
m/z 778.56
m/z 790.54
m/z 804.58
m/z 834.53
m/z 854.67
m/z 888.62
Multivariate segmentation
Low
High
m/z 834.52
m/z 888.62
m/z 281.25
Tissue architecture
B
m/z 778.56
m/z 790.54
m/z 804.58
m/z 834.53
m/z 854.67
m/z 888.62
Cancer
H&E
Tissue architecture
m/z 834.52
m/z 888.62
m/z 281.25
Multivariate segmentation
NAA
m/z 174.04
Additional m/z values
Low
High
m/z 303.23
m/z 681.49
m/z 580.24

Figure S1. DESI-MS imaging suggests that small molecule ions prominent in the healthy tissue are most abundantly present in the sites distal to cancer. (A) DESI-MS ion images (absolute intensity) of prominent healthy tissue lipids identified in Table S1/analyzed in Fig. 1 (with the exception of *m/z* 941.71 that did not produce a good DESI-MS image). These ion images are consistent with distance dependent alteration in abundance reported in Fig. 1 and with two-point laser capture microdissection HPLC-MS (Fig. 1J). A multivariate segmented image (using bisecting k-means on LipoStar MSI[2]) is also included that shows that a unique cluster (green) corresponding to a uniform area surrounding cancer, also populated at the edges of tissue where DESI-MS signal overall shows a drop in intensity. We have also included an overlay of white and gray matter markers (*m/z* 834.52 and *m/z* 888.62[3, 4]). (B) DESI-MS images of ion abundance (absolute intensity) for the same ions in A (Fig. 1) as well as for an additional set of healthy tissue markers are shown here. A segmented image (bisecting k-means clustering) is also included that suggests altered spectral content in the vicinity of cancer. The *m/z* 303.23 (arachidonic acid) has been previously seen using similar DESI-MS experimental conditions by our group[5] and DESI-MS markers of white and gray matter for mouse brain tissue *m/z* 834.52 and *m/z* 888.62[3, 4] have been observed previously by our group[6], reprinted (adapted) with permission. Copyright (2020) American Chemical Society. *m/z* 281.25 (oleic acid) seen previously in other tissues under similar experimental conditions[5] is present in medulloblastoma cancer. The results in this figure are obtained from an independently prepared medulloblastoma bearing brain compared to the specimen studied in Fig.1 (or panel A in this figure). The results are consistent with Fig. 1 observations in that most healthy tissue ions tend to be abundant at sites distal to the cancer region. To investigate the extent to which the biological heterogeneity in the brain structure (distribution of white and gray matter) could explain the trend in abundance seen we have included an H&E image as well as white and gray matter biomarker ions[6] for both Panel A and Panel B tumour cases. The DESI-MS dataset for this specimen has been reported previously[6], reprocessed herein and the previously published H&E images[6] have been reproduced with permission. As can be seen here, the distribution of gray and white matter alone cannot explain the abundance trends seen in many of these ions. The DESI-MS ions used to reveal tissue architecture were visualized with LipoStarMSI[2].

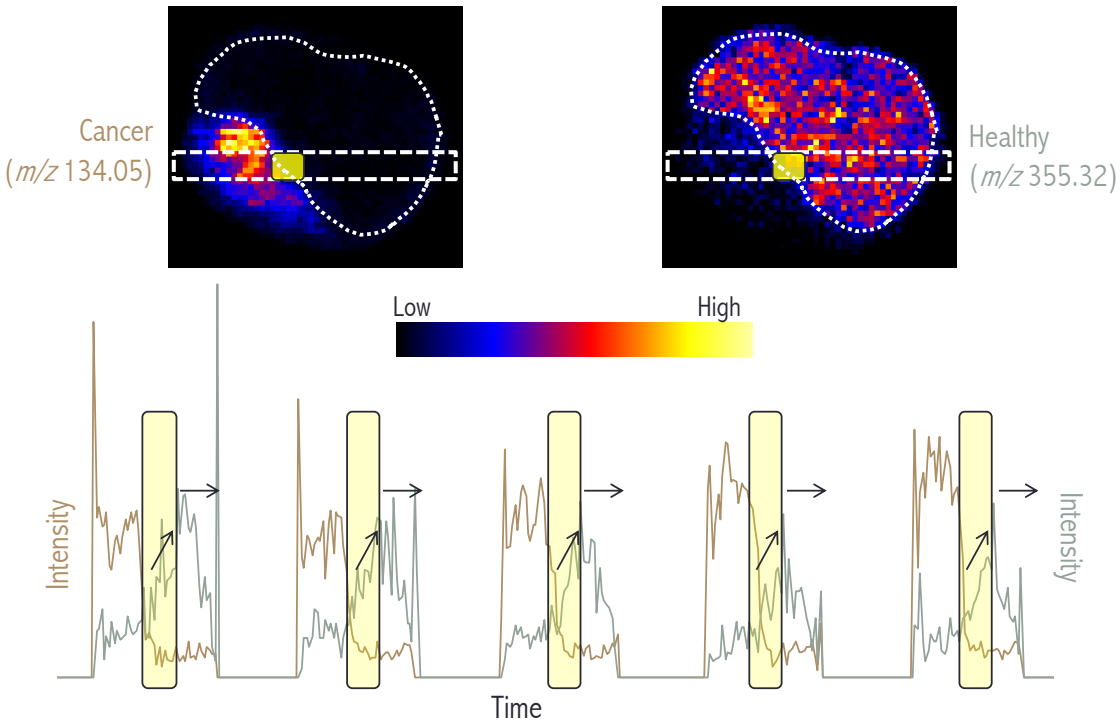

Figure S2. The PIRL-MS imaging of an independent medulloblastoma bearing brain. In this figure we have repurposed the PIRL-MS imaging dataset of a medulloblastoma bearing brain previously published by our group[6], reprinted (adapted) with permission. Copyright (2020) American Chemical Society. Some of the PIRL-MS images presented are published previously[6] and are reproduced here with permission for the clarity of discussion. The highlighted box indicates the transition border between cancer and healthy tissue. The *m/z* 134.05, observed previously in PIRL-MS studies of medulloblastoma[1, 6, 7] and assigned as adenine (*m/z* 134.0473, $C_5H_4N_5^-$)[6, 8], and *m/z* 355.32, previously seen in the healthy tissue[6], are used to denote cancer/healthy tissue boundaries. The border region (boxed) is further highlighted on 5 PIRL-MS line scans wherein a sharp decrease in the intensity of cancer biomarker ion (*m/z* 134.0473, $C_5H_4N_5^-$) [5] is accompanied with a more gradual, gradient-like rise in healthy tissue marker, consistent with the DESI-MS analysis of independent medulloblastoma bearing brain specimen presented in Fig. 1. Therefore, it is highly unlikely that the interactions between the solvent material in a DESI-MS experiment and tissue could explain the distance dependent, ion abundance trends from DESI-MS analyses presented, and discussed in the text.

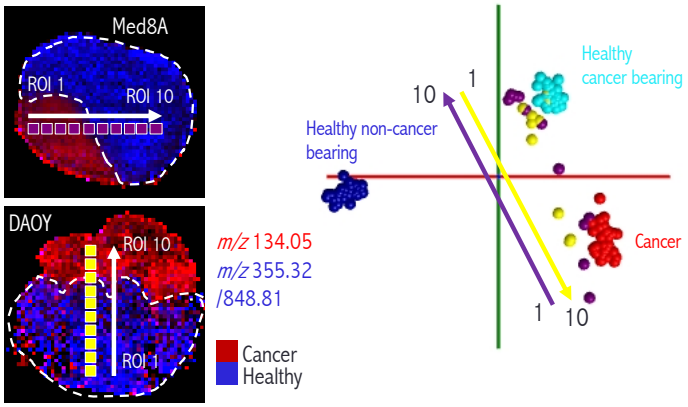

Figure S3. Analysis of ROIs from PIRL-MS images of medulloblastoma bearing brain specimens suggest a cancer-like metabolic state in the healthy tissue regions in the vicinity of cancer. In this figure, we have repurposed the PIRL-MS imaging datasets of two medulloblastoma bearing brain tissues previously analyzed and published by our group[6]. The PIRL-MS images are published[6] and are reproduced here with permission for the clarity of presentation. Copyright (2020) American Chemical Society. The cancer site (red) is highlighted by the distribution of *m/z* 134.05 and the healthy tissue site (blue) is highlighted by the distribution of *m/z* 355.32/848.81 as described previously[6]. The relative position of ROIs with respect to healthy tissue border (highlighted by dashed lines) is indicated. The PCA-LDA model was created using 32 ROIs (9 pixel/ ROI where each pixel covers an area of 200µm by 200µm) from a mixture of DAOY/Med8A bearing brain healthy tissue as well as cancer regions. The PIRL-MS ROIs of the model suggest drastic spectral differences between healthy tissue from cancer bearing or non-cancer bearing brain specimens. More interestingly, the PIRL-MS ROIs from two independent DAOY and Med8A MB cancer bearing brain specimens show a distance dependent, gradient like behaviour with the ROIs close to the cancer border lining up close to the PCA-LDA space occupied by cancer in the model, and those ROIS farther away from cancer border stretching closer to the healthy tissue region of the PCA-LDA model. This observation suggests that no artifactual DESI-MS solvent effects are influencing the validity of conclusions made from DESI-MS results.

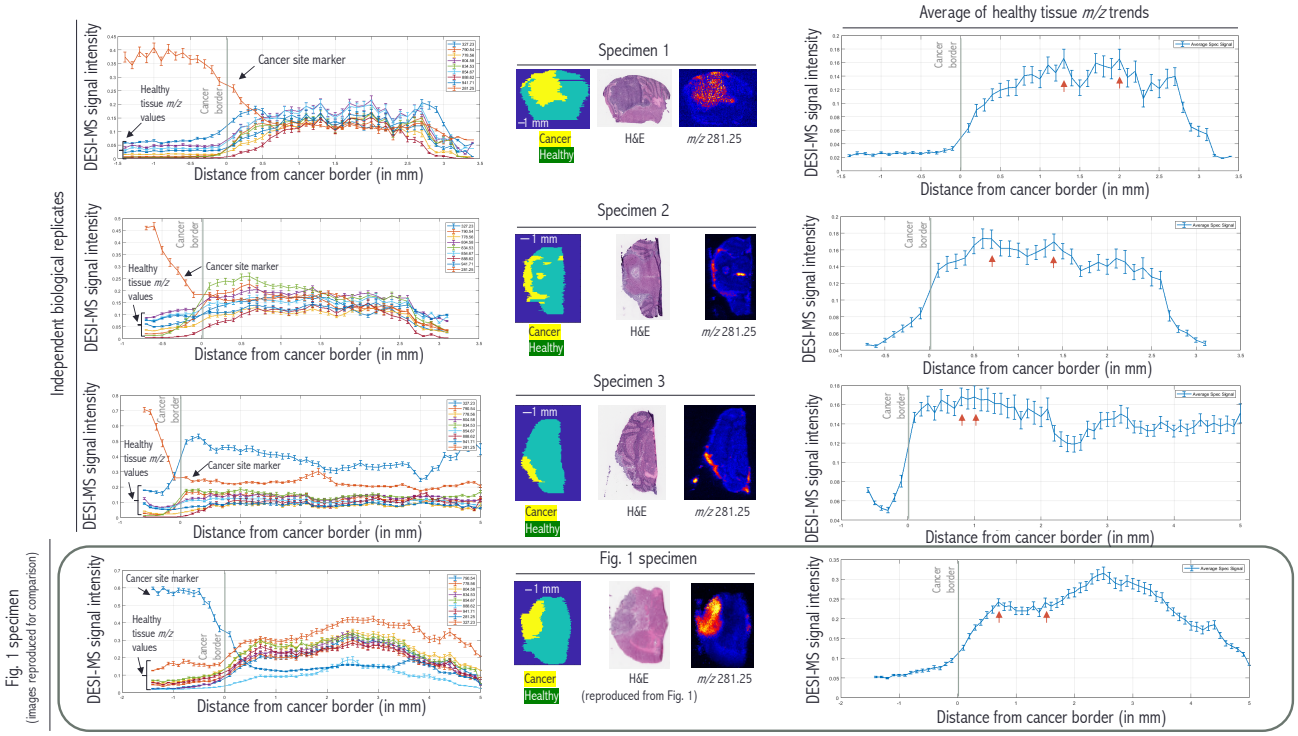

Figure S4. Generality of gradient observation using 3 independent biological replicates of Fig. 1 specimen. In this figure, we are showing the distance dependent gradient across a vector perpendicular to the cancer border as done for Fig. 1 specimen (results presented in Fig. 2) for three independent replicates thereof. For ease of comparison, some of the results presented for Fig. 1 specimen are duplicated here. In addition to healthy tissue ions (*m/z* 778.56, *m/z* 834.53, *m/z* 804.58, *m/z* 941.71, *m/z* 790.54, *m/z* 854.67, *m/z* 888.62) we have also included the gradient trends for DHA (*m/z* 327.23) and its metabolic products (*m/z* 790.54 and *m/z* 834.53). Furthermore, the trends seen for tentative cancer site marker (*m/z* 281.25) is also shown. The same gradient seen in Figs. 1,2 is observed in healthy tissue markers with DHA and its metabolic products conforming to the same pattern consistent with a role for interstitial fluid flow in potentially establishing such a gradient. It is worth noting that the cancer site marker ion's abundance (*m/z* 281.25) sharply decreases at the border. To guide the eye, H&E pathology and manually contoured (segmented) images illustrating cancer site have been included. Additionally, average gradient trends across healthy tissue ions, DHA and its products were also calculated and shown. The plateau region between two consecutive data peaks (marked with red arrows) are shown and suggest 1.3-2.0 mm (specimen 1), 0.7-1.4 mm (specimen 2), 0.8-1.0 mm (specimen 3) and 0.7-1.5 mm (Fig. 1 specimen) from the cancer border.

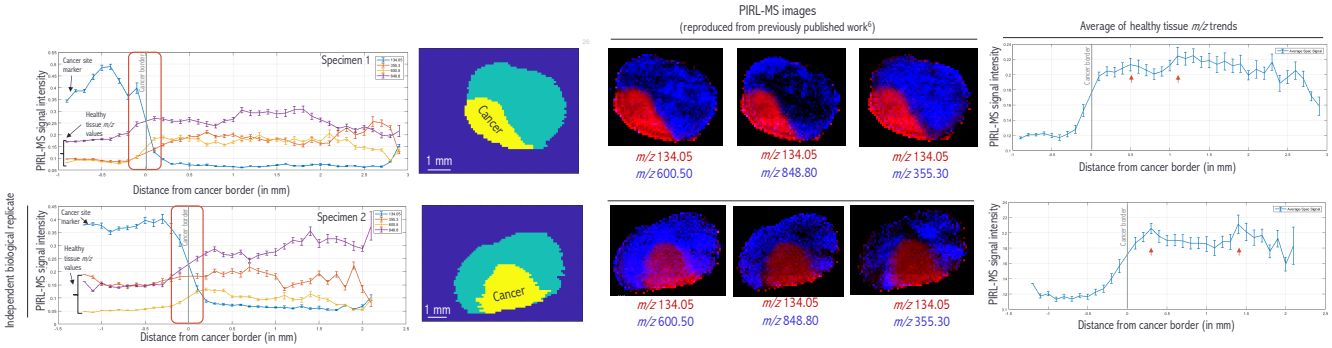

Figure S5. Gradient of healthy tissue markers using PIRL-MS. As *m/z* 281.25 was only a tentative empirically observed and previously not characterized marker for medulloblastoma xenograft cancer, we repeated the Fig. S4 analysis on Fig. S2 specimen and an independent biological replicate thereof, subjected to PIRL-MS analysis as discussed in Fig. S2. The spatial resolution of PIRL-MS is poor compared to DESI-MS utilized in Fig. S4. However, PIRL-MS offers the advantage of a strong cancer site marker. *m/z* 134.05 is a previously studied, identified and established PIRL-MS medulloblastoma cancer maker[6] that decreases very sharply at the cancer border wherein some lag (indicative of gradient seen in Fig. S4) is observed for healthy tissue marker ions (*m/z* 355.30, *m/z* 600.50, *m/z* 848.80). Some of the PIRL-MS images are published previously[6] and are reproduced with permission (Copyright (2020) American Chemical Society). We have presented manually contoured segmented images to guide the eye to the cancer region used in the analysis of gradient plots. Albeit limited by the poor spatial resolution of PIRL-MS, a similar gradient behaviour along a vector perpendicular to the cancer border is seen wherein, average gradient trends across healthy tissue marker ions (*m/z* 355.30, *m/z* 600.50, *m/z* 848.80) suggest a signal plateau at 0.5-1.1 mm and 0.3-1.4 mm away from the cancer border.

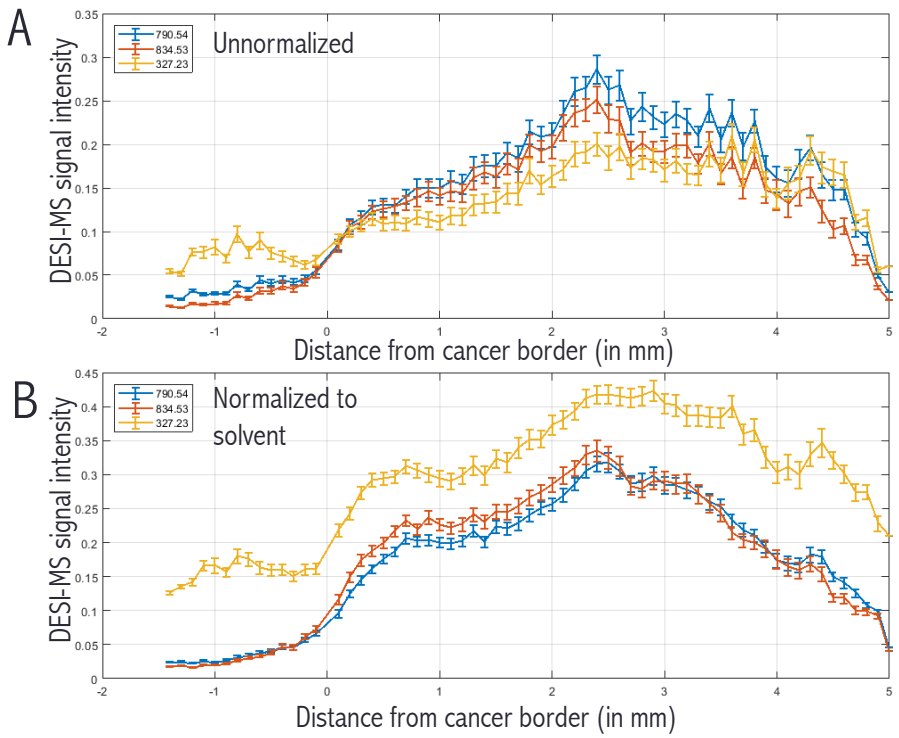

Figure S6. The ion abundance trends for DHA and DHA containing lipids across a vector perpendicular to the cancer border. In this figure, we have extended the same analysis of Fig.2 to DHA (*m/z* 327.23) and DHA containing GPLs *m/z* 790.54 and *m/z* 834.53 (See Table S1 for identity assignments). We show the abundance patterns for these ions across a 5 mm distance along a hypothetical flow vector perpendicular to the cancer border. The pattern of abundance for these three ions unnormalized (A) and normalized (to solvent *m/z* 283.23) in panel (B) are presented and shown to be coinciding. While all these ions conform to the expected pattern of gradient as recovered for Fig. 2 over the short 1.2 mm distance, they additionally show concordance in their abundance patterns across the larger 5.0 mm range. While interpretation of the second rise in signal at 2.5 mm and subsequent fall towards the 5.0 range is difficult (and is likely compounded by potential influence of healthy brain tissue heterogeneity on these length scales (See H&E in Fig.1A), the concordance of the pattern seen, nevertheless, is something that is expected for the metabolic product ions of a precursor molecule. This observation is consistent with alterations in DHA abundance along a perpendicular diffusion vector being mirrored in DHA containing lipids *m/z* 790.54 and *m/z* 834.53. In this figure, the error bars indicate 10% of the standard deviation at each distance from the boundary. Values are normalized to lie between (0,1) prior to calculating the average to visualize their relative behaviours along the gradient. Negative distances are those within the tumour, with positive distances traveling outwards. Therefore, each plot represents the average change in spectra strength as moving from a point on the tumour's medial axis outwards on a straight line along the tumour contour's normal to a distance of 5.0 mm.

Controls

Tissue density alterations

Previous studies from our group suggested that the abundance of lipids in an MS image could be modulated by tissue density variations in the pixels examined, wherein a lower tissue density could result in an artificially lower abundance of lipids[9]. Therefore, only in the absence of drastic variations in tissue density across a specimen could changes in lipid abundances such as those reported in the observed gradient be confidently related to altered metabolic states[9]. Therefore, we performed tissue density calculations on the specimen analyzed in Fig. 1 as described previously[9]. As shown below there were no aberrant alterations in tissue density that could account for the low abundance of lipids in the vicinity of the cancerous region. Tissue density in the region of intermediate NAA abundance ~1.2 mm from the cancer border had a value of 0.80±0.07. This density value is very close to the extracted density estimate of 0.86±0.07, determined over the entire healthy tissue outside the NAA transition zone. Furthermore, no gradient of tissue density to explain the gradient in the abundance of tissue lipids, as reported in Fig. 1F, was detected in the region of intermediate NAA abundance.

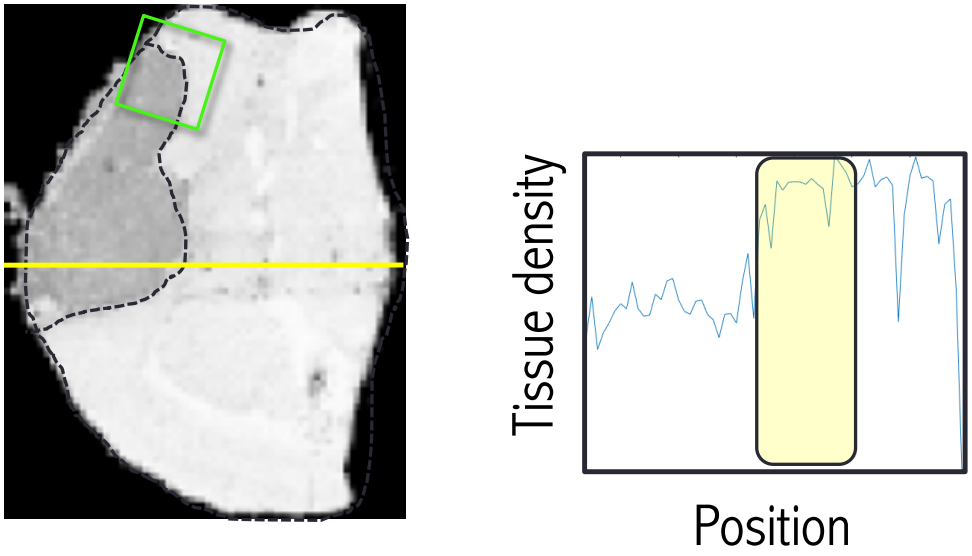

Tissue density map. Tissue density map[9] suggests no drastic alteration of tissue density in the NAA abundance 'transition zone' that could rationalize the distance-dependent gradient of increased abundance as a function of increased distance from the cancer border. The tissue density across the arbitrary scan line (yellow) suggests no intermediate tissue density in the area of NAA intermediate abundance (highlighted).

Hypoxia

It is known that hypoxia may alter lipid metabolism in cancer cells[10] including the brain[11, 12]. Immunohistochemistry analysis reporting on the abundance of carbonic anhydrase enzyme, itself a hypoxia marker[13], was performed. As judged by the low level of positively stained cells (brown stain), the cancer region was deemed to be normoxic in the specimen analyzed in Fig. 1. As hypoxia is known to result in drastic changes in the lipidome[14] accessible with DESI-MS [15] it is unlikely that the cancer-like metabolic states seen in the vicinity of a non-hypoxic tumour to be

due to hypoxia. We were also unable to detect any of the proposed hypoxia DESI-MS markers[15] in our dataset.

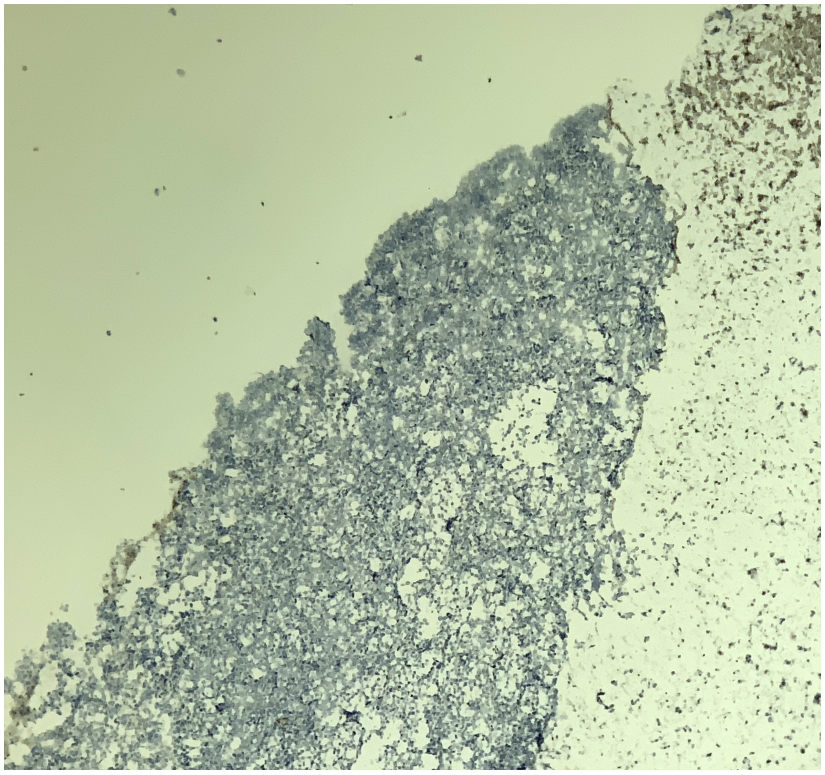

Hypoxia staining. Carbonic anhydrase stained image of the tissue, suggesting no hypoxia in the cancer region. The region shown is highlighted with a green box on the tissue density map above. The antibody used showed no cross reactivity to mouse to directly report on the hypoxia status of the healthy tissue in the vicinity of cancer. However, in the absence of a hypoxic tumour we strongly believe that the surrounding healthy tissue is normoxic. The hypoxic regions are expected to appear as brown stain. The blue (darker) background indicates cancer cells that possess large nuclei. No brown stain indicative of hypoxia was detected.

Edema

A confounding factor that prevents us from putting forward a detailed mechanistic explanation for our observation is that residual immune response and swelling of the brain (edema) may occur in xenografts, leading to additional alterations of the metabolic state. While edema is not necessarily expected to possess cancer-like metabolic states, its effects may be observable across the entire specimen. In our tumour bearing DESI-MS dataset used in Figs. 1,2, however, the abundance of known ischemia and macrophage markers indicative of immune response[16] resembled the basal levels detected in healthy tissue from non-tumour bearing mice (Panel A) While the absence of ischemia or macrophage markers may not necessarily rule out edema, no spatially localized abundance of such markers were seen outside the tumour region. Likewise, we found no evidence of *m/z* 572.48 marker ceramide $[Cer(d34:1) + Cl]^-$ a widely seen necrosis marker[5, 17-19] being associated with the region of intermediate NAA abundance (Panel B).

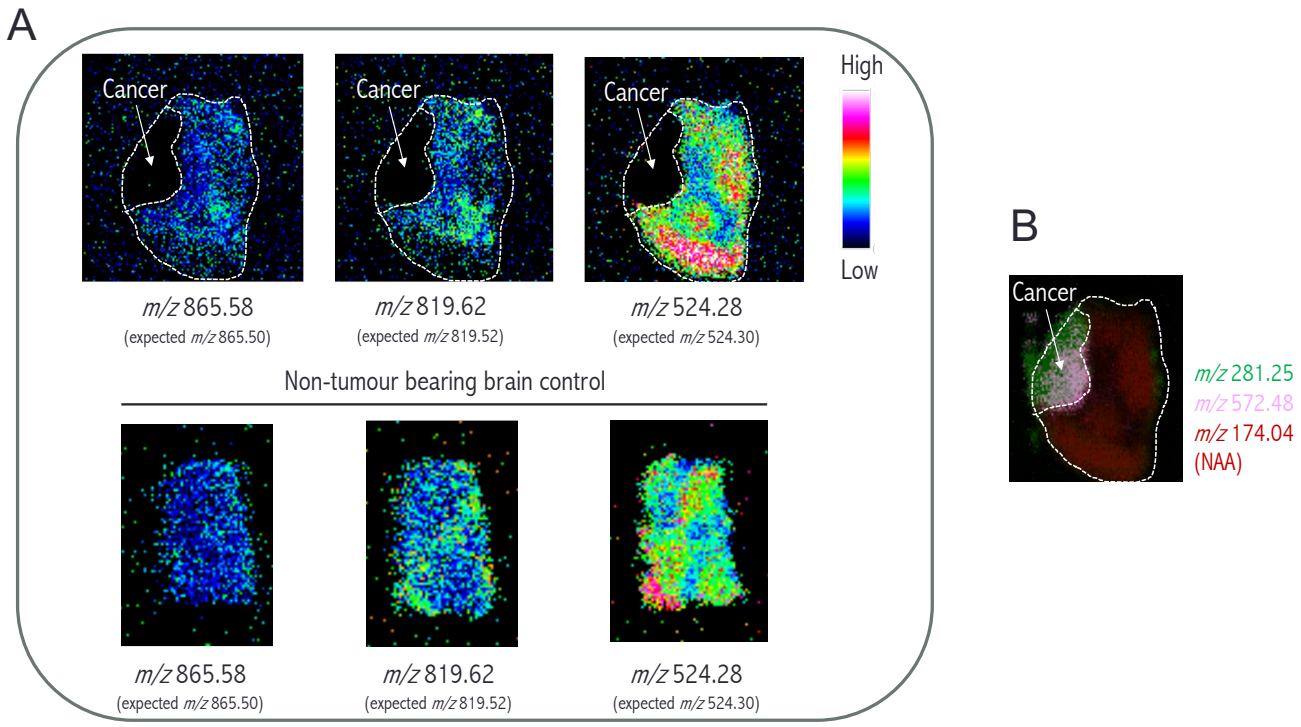

Assessment of ischemia and cell death in DESI-MS dataset analyzed in Figs 1,2. Presence of cancer can cause tissue inflammation, edema or trigger ischemia processes. To ensure that the region of NAA intermediate abundance showing the gradient of cancer-like metabolic state (i.e. healthy tissue adjacent to the cancer border) is not artifactually populated with necrotic or ischemic cells, we inspected the DESI-MS dataset for the presence of previously established mass spectrometry markers of ischemia or necrosis. (A) Known markers of ischemia[16] and macrophage accumulation bis(monoacylglycero)phosphate (BMP) *m/z* 819.52 [BMP (40:7)] , *m/z* 865.50 [BMP (22:6/22:6)] and *m/z* 524.30 [LysoPS (18:0)] show abundances that are comparable to those seen in non-tumour bearing brain specimen. None of these markers are localized to the area of intermediate NAA abundance where a gradient of cancer-like metabolic states is seen arguing against inflammation or immune response to play a factor in affecting our observations.(B) The *m/z* 572.48 $[Cer(d34:1) + Cl]^-$ (necrosis marker[5, 17-19]) is only seen inside the tumour region and is absent from the NAA intermediate abundance as well as the rest of the tissue. In both panels normalized (to TIC) ion images are shown using LipoStar MSI[2]. For Panel A results we have also listed the expected mass of ions upon transfer of assignment from published results to what we have seen in our DESI-MS spectra. The uncertainties associated with this tentative transfer are highlighted and can influence the interpretations. The publication used as a guide[16] lists additional ion markers of ischemia but those were not detected in our results. While this cannot be taken to rule out ischemia, inflammation or edema *per se*, the very low relative abundance of those ions that were detectable (relative to healthy brain tissue) strongly argues against inflammation at the edge of the tumour influencing our molecular readout.

Directionality of the gradient trend

The panels below show the DESI-MS ion abundance patterns along vectors parallel to the cancer border for both unnormalized (Panel A) and solvent normalized values (Panel B). We chose an isocontour line 0.3 mm away from the cancer border (Panel C) where we expected the flow influence on ion abundance to be present (See Fig.2). Intensities along this vector, perpendicular to the diffusion flow vector, are not expected to be drastically influenced by the presence of an outward flow which by definition is perpendicular to the cancer border. Consistent with this, such data points do not conform to the gradient pattern recovered in Fig. 2 for those collected along the expected direction of the interstitial fluid flow vector, assuming it existed.

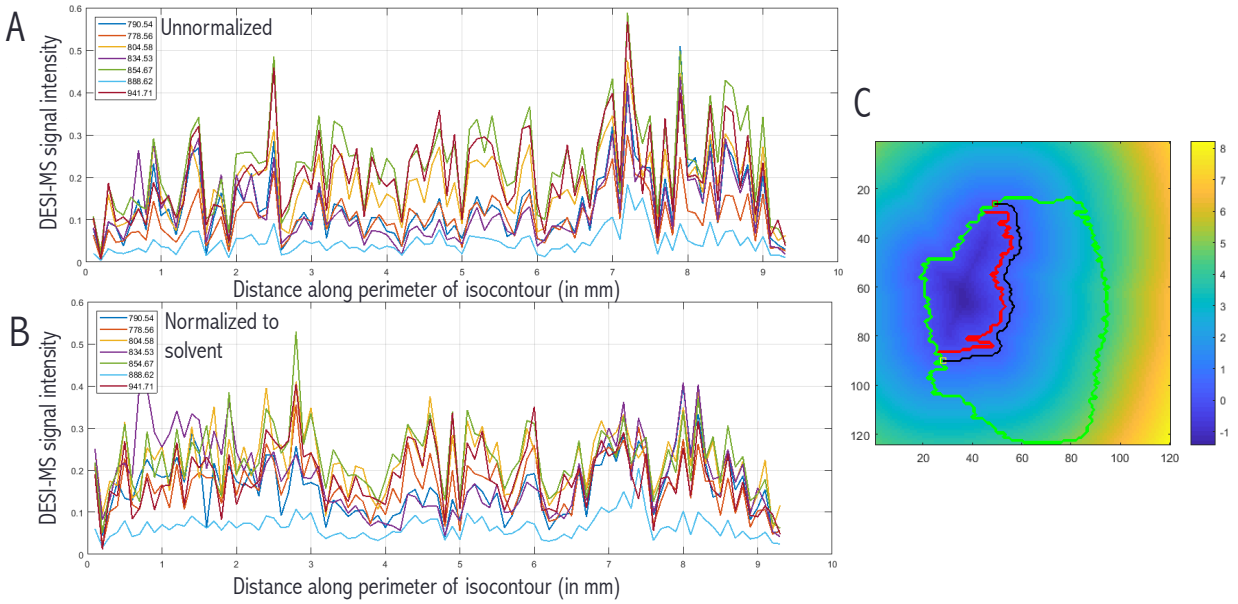

The abundance of DESI-MS ions perpendicular to the direction of the proposed interstitial fluid flow. In this figure we are presenting the DESI-MS signal strength of the healthy brain tissue ions (Table S1) along an isocontour 3 pixels (0.3 mm) away from the cancer border where from Fig. 2 we observed the gradient like behaviour parallel to the direction of the flow (or perpendicular to the cancer border). DESI-MS signal strength for both (A) unnormalized and (B) solvent normalized (See Fig. 2 legend) is presented. Panel C represents distance from the closest point on the tumour boundary where the green line represents the tissue border, red line indicates the cancer boundary and the black line shows the isocontour line used in panels A,B for the analysis. This line was traced from the red square towards the yellow square for this analysis. No gradient-like behaviour was seen perpendicular to the expected direction of the interstitial fluid flow (or parallel to the direction of the cancer border isocontour line examined).

Statistical modeling

To further evaluate whether the gradient of the metabolic state(s) seen in Figs. 1F and 2 from a single 2D tissue slice will hold true over other independent tumours, we first prepared an independent orthotopic medulloblastoma bearing brain, then serially sectioned it to clear the cancer region entirely and analyzed both the proximal (containing cancer) and distal (clear of cancer) sections thereof with DESI-MS imaging. We further collected average DESI-MS spectra from 10-pixel (0.01 mm^2) regions of interest (ROIs) from two types of morphometrically equivalent healthy tissues: (1) healthy tissue from non-cancer bearing mouse brain and (2) healthy tissue distal to the cancer site from a second independently prepared tumour bearing mouse brain. We then subjected the average spectra of each ROI to principal component analysis-linear discriminant analysis (PCA-LDA) modeling, as previously performed to interpret the spectral (and hence metabolic) similarities between different biological specimens[20]. All panels show the PCA-LDA scores plots where each data point corresponds to the DESI-MS spectrum of an ROI. Here, the data points that possess similar mass spectra will form a closely grouped cluster in the PCA-LDA space. Consistent with the HPLC-MS results (Fig. 1J), the healthy tissue ROIs from tumour bearing mouse brain had a drastically altered metabolic state (as judged by differences in their DESI-MS spectra) compared to the healthy tissue ROIs from non-cancer bearing mouse brain. Therefore, morphometrically identical healthy tissues are seen to possess very different metabolic profiles based on whether cancer cells are present in their vicinity.

We additionally collected DESI-MS spectra according to a gradient of distances across the DESI-MS image of the proximal tissue section described above. The DESI-MS spectra of the healthy tissue ROIs obtained along a gradient of distances from the cancer region contained mass spectra that also showed a gradient of similarities with those of the ROIs from cancer and healthy tissue regions of the independent tumour bearing mice. Strikingly, the same regions of the PCA-LDA space occupied with the gradient data points described above could be populated with artificially created mixed DESI-MS pixels containing a gradient of cancer and healthy tissue metabolic contents (panel B). This control experiment was performed to provide further support that the distance-dependent gradient data points reported in panel A contained a gradient of cancer-to-healthy-like metabolic profiles. The support for this statement comes from the co-incidence of data points with known cancer/healthy dual character (shown in panel B) falling in the same regions on a PCA-LDA scores plot as the data points gathered along a gradient of distances from the cancer border (shown in panel A). To put this co-incidence to the test, we further sectioned the same cancer-bearing brain to obtain a tissue slice that was sufficiently far (>1.2 mm) away from the cancer border and then collected ROIs from this distal slice in the same manner as for panel A. In the PCA-LDA modeling of the DESI-MS spectra of ROIs from this distal section (>1.2 mm away from cancer) no such gradient was seen (Panel C). All ROIs from this specimen were equidistant, and sufficiently (>1.2 mm) far from the cancer region to the point that their metabolic states could not have been influenced by the presence of cancer in the proximal specimen analyzed in panel A. This observation is consistent with our results above in showing that distance-dependent alterations in the tissue metabolic state are taking place only in the vicinity of cancer. Further to this, it must be noted that PCA-LDA modeling utilizes highly specific molecular changes captured over the entire small molecule range of the mass spectra including metabolome and lipidome. The results of the PCA-LDA modeling scores plots taken together with the specificity of PCA-LDA analysis further reinforce the notion that healthy tissue cells in the vicinity of cancer possess cancer-like metabolic states.

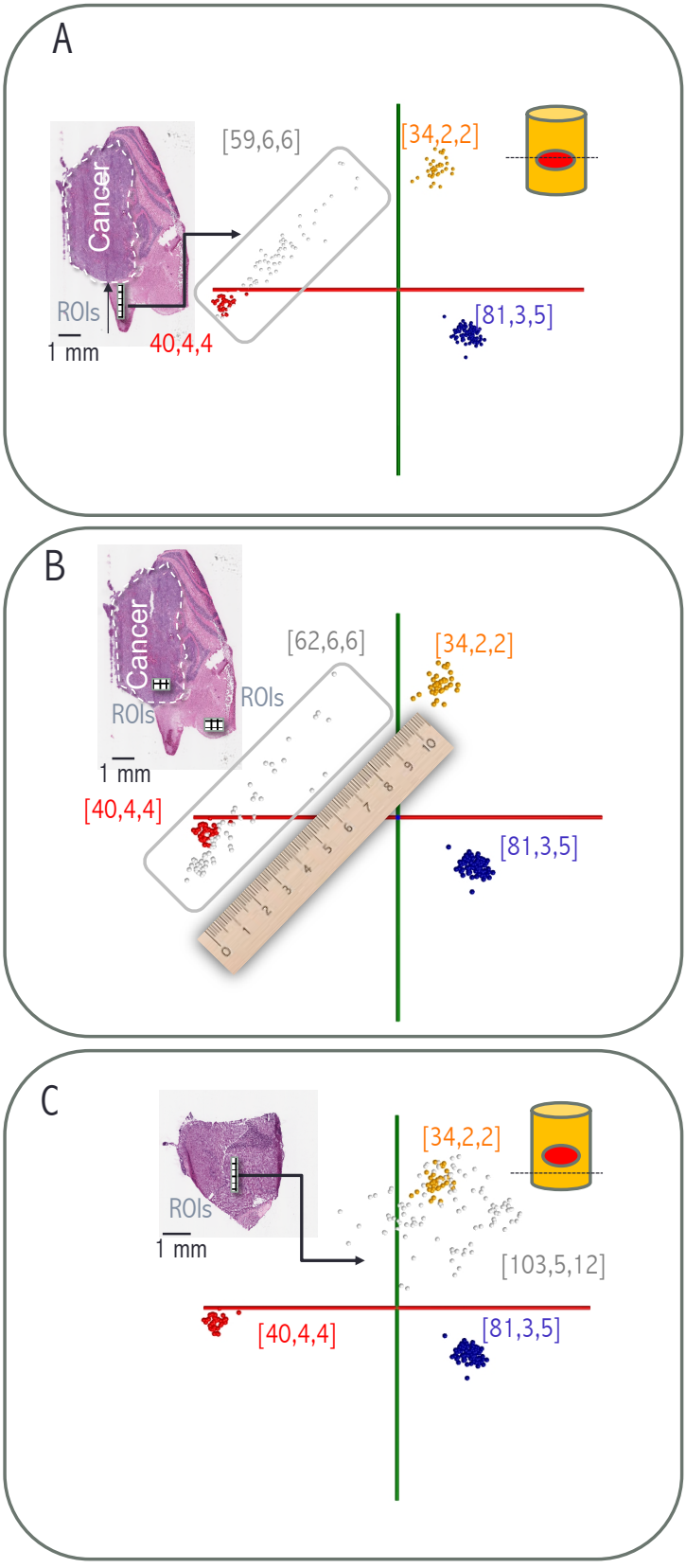

[ROIs, slides, sections]
Healthy tissue ROIs from non-cancer bearing brain
Healthy tissue ROI from independent cancer bearing brain
Cancer tissue ROIs from independent cancer bearing brain

Statistical modeling of the DESI-MS spectra from cancer adjacent healthy tissue suggests a cancer-like metabolic state. (A) Distribution of 59, 10-pixel ROIs from a gradient of distances from the cancer border averaged from 6 tissue slices present on 6 independently imaged slides. The data points on the PCA-LDA space (scores plot) arrange themselves along an axis that stretches from the cancer data points of the model to the healthy tissue from said independent cancer bearing brain. (B) Overlay of 62, 10-pixel ROIs created from mixing different ratios of healthy and cancer single pixels from same 6 slices (on 6 independently imaged slides) described above using the same PCA-LDA model (scores plot) shown in Panel A. Interestingly, these artificially mixed pixels that possess varying degrees of both cancer and healthy tissue characteristics align themselves in the same area of the PCA-LDA space as those shown in panel A scores plot occupied with distance-dependent ROIs from healthy tissue. This area is highlighted by a box. This coincidence suggests that distance-dependent ROIs sampled in panel A indeed possess cancer-like spectral and hence metabolic similarity. (C) The same model used to evaluate the PCA-LDA space localization of 103, 10-pixel ROIs from 12 tissue slices present in 5 independently imaged slides containing a distal section that is sufficiently far away (>2 mm) from the cancer. As can be seen here, these query ROIs aligned themselves in close proximity of healthy tissue from cancer bearing brain and no longer on the observed gradient line seen in panel A and contextualized with the 'ruler' gold standard control of mixed pixels in panel B. A non-copyrighted image of a generalized ruler is used to convey this point. We have depicted a cartoon representation of how tissue sectioning for slices analyzed in panels A and C related to the volume of cancer bearing brain tissue blocks used for sectioning. In panel A, the section is made inside the cancer region and in panel C outside of it. For this figure we first created a statistical model from 10 pixel (0.01 mm^2) ROIs from cancer and healthy regions of the tissue slice analyzed in Fig. 1. The model consisted of 40, 10 pixel ROIs across four cancer slides each containing 1 tissue slice independently acquired to show concordance; 34 ROIs of healthy tissue >1.2 mm from cancer (sufficiently far from the cancer border not to involve the NAA abundance 'transition zone' shown in Fig. 1B,D) averaged from two slides each containing a single slice independently imaged; and 81 ROIs from healthy non-cancer bearing brain from a total of 5 slices available within 3 independently imaged slides. From the modeling results, healthy tissue from cancer-bearing brains possesses a drastically different mass spectral content compared to the healthy tissue from non-cancer bearing brains and the cancer tissue itself.

To further investigate whether limited (changes in a few *m/z* values) or global (changes of identity or abundance across *m/z* values) alterations in the mass spectra account for the molecular heterogeneity of cancer-neighbouring healthy tissue ROIs analyzed in above, we created a different PCA-LDA model that describes the statistical discrimination between DESI-MS spectra of (1) cancer-adjacent healthy tissue, (2) cancer, and (3) healthy tissue from tumour bearing mouse brains. We then inspected the model's loading plots that summarize the relative rank of each *m/z* contribution across the entire mass spectrum to the statistical discrimination seen. The PCA-LDA scores plot for this model is comprised of distinctly grouped data clusters suggesting they contain distinct mass spectral properties. The inspection of the loading plots associated with this PCA-LDA model confirms global contributions of many *m/z* values to the statistical discrimination seen. Therefore, cancer-adjacent healthy tissue cells contain a distance-dependent gradient of distinct metabolic states associated with global changes in mass spectra.

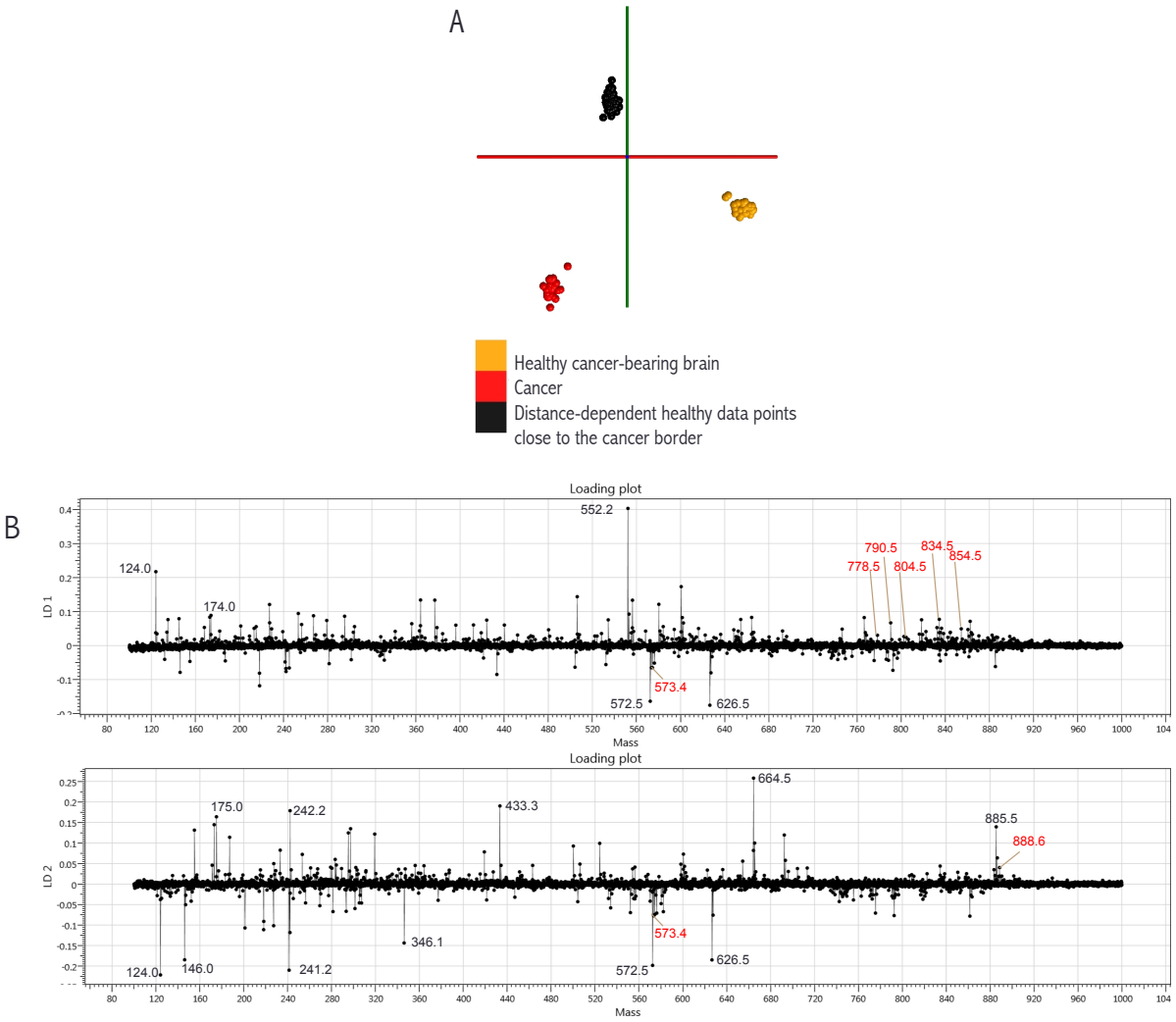

PCA-LDA modeling suggests global metabolic changes in healthy cells close to the cancer border. In this figure we repurposed the data presented above as part of a new PCA-LDA model. This model highlights the statistical discrimination of DESI-MS spectra from ROIs collected across a gradient of distances from the cancer border compared to those from the cancer site and healthy tissue from cancer-bearing mouse brain. (A) PCA-LDA scores plot. Here, a clear statistical discrimination between said data groups is seen. (B) PCA-LDA loading plots across two linear dimensions (LD1 and LD2). Here, the LD1 plot denotes the axis (red line) of statistical discrimination between cancer and healthy tissue where some of the distinguishing ions reported in Table S1 (highlighted in red) are seen, as expected. These ions, however, while present are not major contributors to the statistical discrimination along this axis. The LD2 plot, on the other hand, denotes ions that distinguish the gradient-dependent data points from either of the cancer or healthy tissue groups. The collective patterns seen in the LD1 and LD2 loading plots suggest global changes in many *m/z* values. Therefore, the statistical discrimination between the gradient-dependent data points and the cancer and healthy tissue groups seen are not being driven strongly by a specific ion, and the gradient data points group between the cancer and healthy tissue points along the main axis of separation.

To ensure that the supervised nature of the PCA-LDA analysis did not result in overfitting, we performed unsupervised hierarchical clustering of this model. We further show that the healthy brain tissue from cancer bearing mice formed its own cluster away from the healthy brain tissue from non-cancer bearing mice after hierarchical clustering despite inter-sample heterogeneities resulting in further dissection of the cancer data points into own clusters.

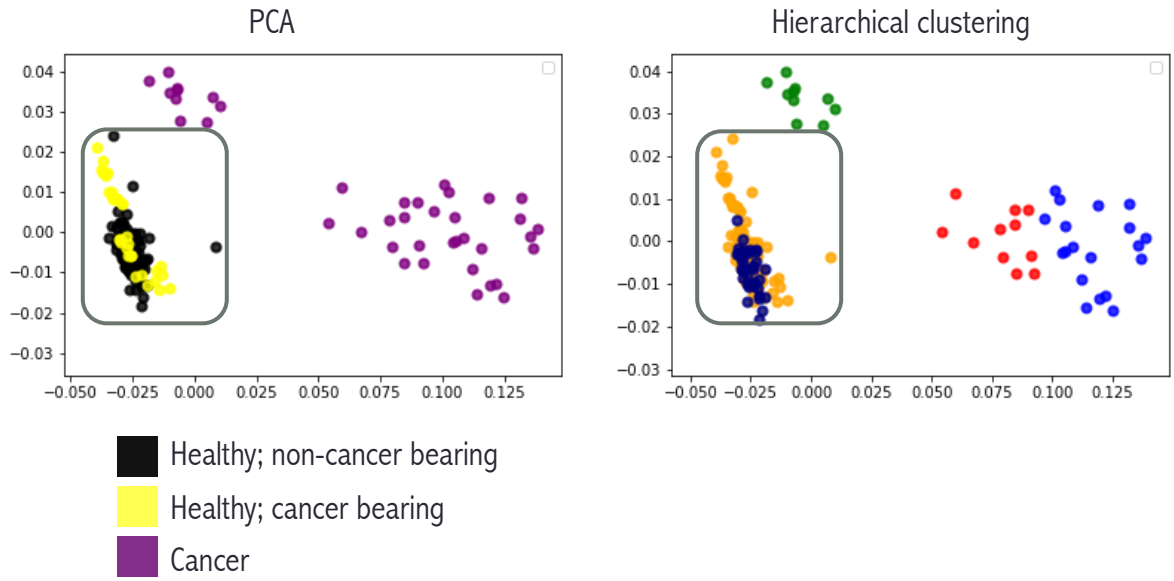

Unsupervised hierarchical clustering of PCA-LDA model. In this figure we performed PCA as well as hierarchical clustering of the supervised model above comprising data points from cancer, healthy tissue from cancer-bearing and non-cancer-bearing mouse brain specimens. The boxed area contains data points that correspond to healthy tissue. Hierarchical clustering results suggests two clusters in the healthy tissue region (boxed). Comparison with the corresponding PCA plot suggests that the two clusters seen are largely contributed to by the difference in DESI-MS spectra of healthy tissue from tumour bearing and non-tumour bearing mice. In this plot, PCA as well as hierarchical (displayed on PCA) clustering results (5 clusters) have been shown. PCA itself suggests additional inter-sample variability in the cancer data points where a 'separate' grouping of DESI-MS data points from different tissue slices was seen (e.g. green cancer cluster corresponds to data collected from one tissue slide where a total of 4 slides were used in making the model). The overlap seen between the signatures of healthy brain tissue regions from cancer-bearing and healthy mice in the PCA plot (boxed area) can be resolved through hierarchical clustering. A caveat here is that the cancer data points that contain significant intersample variability are also dissected into additional clusters.

Experimental Methods : Additional details

Principal Component Analysis – Linear Discriminant Analysis (PCA-LDA)
PCA-LDA modeling was performed using Waters Abstract Model Builder (AMX) version 1.0.1360.0. The model was built using DESI-MS data by exporting the average spectra from a series of 10-pixel regions of interest (ROIs) using the "export as MassLynx raw data" function in Waters HDI software. These were imported into AMX in the same manner as described previously for data collected using PIRL-MS[20]. As each file is an averaged spectrum, there is no need to select a scan range on the "sample list" tab but instead the "one spectrum per sample" box should be checked under the "spectrum interpretation" section of the "model properties" tab. The model was built with 30 PCA dimensions (~1/5 of the 155 total spectra) and 2 LDA dimensions (the maximum available), as previously used by our group[20] (note than none of the model properties were deliberately optimized to result in biased statistical discrimination between data groups). Mass range was 100-1000 Da and the binning was set to 0.1Da. Parallel model building with binning windows of 0.3 and 0.5Da resulted in little to no significant impact on the clusters. These values were consistent with previous successful classifications in the context of peak resolving power of the instrument used[1]. Solvent ions were excluded from the model using the "exclusion list" feature of AMX, these ions were selected by comparing the spectrum collected from outside the tissue region (i.e. the background) of 5 different slides and compiling a list of all the ions common to the background of each slide. In this way, we aimed to avoid excluding ions that may originate from tissue fragments that could exist outside the main tissue area as a result of the sectioning process. The data points in gray displayed on the models were not built into the models themselves. After the model had been constructed (using the settings above) the data points to be displayed were imported under the sample list tab and, on the same tab, these points were selected and the "add to list" button under the "spectrum operations" section was used to display them on the model visualization field. In this way, these points are displayed as though the model was classifying them, rather than being part of the model's construction. Solvent peaks were excluded from PCA-LDA analysis of samples with DESI-MS.

Unsupervised clustering analysis
Hierarchical clustering using an in-house Python based program was performed as described previously[6]. The script used an Agglomerative Clustering object equipped Scikit learn library to perform bottom-up hierarchical clustering. Observations began in their own clusters which were then merged together successively. Ward Linkage was used to minimize the sum of squared differences between all the clusters.

Laser Capture Microdissection (LCM)
LCM was performed using the MMI Cell Cut system (Nikon Microscopies). Fresh-frozen brain tissue was cut into 10µm sections as described for DESI-MS imaging above, but instead of transferring to a glass slide, sections were transferred to the flat side of MMI membrane slides®. Slides were stored at -80^{o}C until ready for LCM. The MMI CellTools software was used to select regions of 2mm^2 area for automated cutting and collection into a special 0.5mL collection tube with a diffuser cap (MMI). The membrane on the cap sticks to the membrane above the cut region of tissue, such that the face of the tissue not covered by membrane faces down into the tube for lipid extraction.

LC-MS and MS/MS analysis

Extraction of lipids from LCM tissue for HPLC-MS and MS/MS was performed using 1mL of chloroform as described previously [1]. The mass spectrometer and source parameters were unchanged. The MS scan was acquired in a range of *m/z* 400-1000 Da. Accurate mass was obtained by the lock mass mode with a reference ion (*m/z* 554.2615) of Leucine-Enkephalin. For the chromatographic separation: the solvent used for sample reconstitution was isopropanol:acetonitrile:water (4:3:1, v:v) and the chromatographic column was a Waters Acquity UPLC CSH C18 column (2.1 X 100mm, 1.7µm) at 55° C. A gradient was established between mobile phase A (water:acetonitrile 2:3 with 10 mM ammonium formate and 0.1% formic acid) and mobile phase B (isopropanol:acetonitrile 9:1 with 10 mM ammonium formate and 0.1% formic acid) with phase A run at 100% for the first 5 minutes, 50% for the next 12 minutes, 30% for 0.1 minutes and 0% (i.e. 100% B) for the next 0.9 minutes. The run finished with 100% phase A for the last two minutes. MS/MS scan was acquired in a range of m/z 50-1000 Da with scan time of 0.3 s. The typical collision energy ramps were 30-45 V, 40-60 V and 50-70 V for *m/z* <800, *m/z* 800-850 and *m/z* >850, respectively. All other conditions were as previously reported [1]. The box plots in Fig. 1J were generated using the program MetaboAnalyst [6] using the two column (retention time & base peak intensity) HPLC-MS data. The tissue regions highlighted in Panel A were subjected to laser capture microdissection for this analysis.

Digital Pathology

Digital pathology methods all used the Definiens (Munich Germany) software, with 20x resolution H&E images uploaded for analysis. Details of the file processing and initial settings can be found in [9]. Tissue density calculations used a slightly modified version of the Definiens Developer Ruleset used in the previous work[9]. Rather than performing image registration on the spatially referenced aggregate statistics file, image registration of the H&E section to the MS image were performed prior to analysis. Furthermore, tissue area is defined as the total area of each tile, subtracting the area covered by nuclei or empty space. Internal validation has found no differences in analysis results using either methodologies. The degree of cancer infiltration in healthy tissue was investigated on the same platform utilizing a nuclear size cut off value of 60µm^2, where larger cells were classified as cancer, and smaller as healthy.

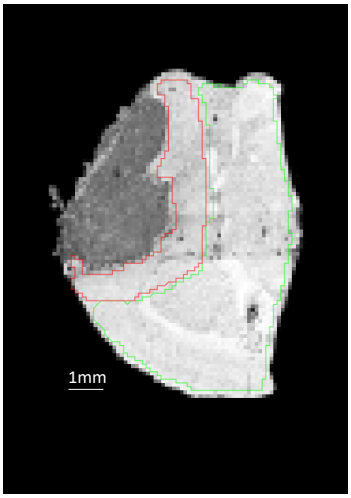

Digital pathology masks. In this figure, we are showing tissue masks used for the estimations of tissue density between NAA transition zone (intermediate abundance, denoted by the red mask) and the rest of the healthy tissue (denoted by green mask). The masks are shown (arbitrarily) on an expanded view of the tissue density plot which is presented in the Control section.

References:

1. Woolman, M.; Kuzan-Fischer, C. M.; Ferry, I.; Kiyota, T.; Luu, B.; Wu, M.; Munoz, D. G.; Das, S.; Aman, A.; Taylor, M. D.; Rutka, J. T.; Ginsberg, H. J.; Zarrine-Afsar, A., Picosecond Infrared Laser Desorption Mass Spectrometry Identifies Medulloblastoma Subgroups on Intrasurgical Timescales. *Cancer Res* **2019,** *79* (9), 2426-2434.
2. Tortorella, S.; Tiberi, P.; Bowman, A. P.; Claes, B. S. R.; Scupakova, K.; Heeren, R. M. A.; Ellis, S. R.; Cruciani, G., LipostarMSI: Comprehensive, Vendor-Neutral Software for Visualization, Data Analysis, and Automated Molecular Identification in Mass Spectrometry Imaging. *J Am Soc Mass Spectr* **2020,** *31* (1), 155-163.
3. Eberlin, L. S.; Ferreira, C. R.; Dill, A. L.; Ifa, D. R.; Cheng, L.; Cooks, R. G., Nondestructive, histologically compatible tissue imaging by desorption electrospray ionization mass spectrometry. *Chembiochem : a European journal of chemical biology* **2011,** *12* (14), 2129-32.
4. Campbell, D. I.; Ferreira, C. R.; Eberlin, L. S.; Cooks, R. G., Improved spatial resolution in the imaging of biological tissue using desorption electrospray ionization. *Analytical and bioanalytical chemistry* **2012,** *404* (2), 389-98.
5. Tata, A.; Woolman, M.; Ventura, M.; Bernards, N.; Ganguly, M.; Gribble, A.; Shrestha, B.; Bluemke, E.; Ginsberg, H. J.; Vitkin, A.; Zheng, J.; Zarrine-Afsar, A., Rapid Detection of Necrosis in Breast Cancer with Desorption Electrospray Ionization Mass Spectrometry. *Sci Rep* **2016,** *6*, 35374.
6. Katz, L.; Woolman, M.; Talbot, F.; Amara-Belgadi, S.; Wu, M.; Tortorella, S.; Das, S.; Ginsberg, H. J.; Zarrine-Afsar, A., Dual Laser and Desorption Electrospray Ionization Mass Spectrometry Imaging Using the Same Interface. *Anal Chem* **2020,** *92* (9), 6349-6357.
7. Woolman, M.; Ferry, I.; Kuzan-Fischer, C. M.; Wu, M.; Zou, J.; Kiyota, T.; Isik, S.; Dara, D.; Aman, A.; Das, S.; Taylor, M. D.; Rutka, J. T.; Ginsberg, H. J.; Zarrine-Afsar, A., Rapid determination of medulloblastoma subgroup affiliation with mass spectrometry using a handheld picosecond infrared laser desorption probe. *Chem Sci* **2017,** *8* (9), 6508-6519.
8. Passarelli, M. K.; Pirkl, A.; Moellers, R.; Grinfeld, D.; Kollmer, F.; Havelund, R.; Newman, C. F.; Marshall, P. S.; Arlinghaus, H.; Alexander, M. R.; West, A.; Horning, S.; Niehuis, E.; Makarov, A.; Dollery, C. T.; Gilmore, I. S., The 3D OrbiSIMS-label-free metabolic imaging with subcellular lateral resolution and high mass-resolving power. *Nat Methods* **2017,** *14* (12), 1175-1183.
9. Bilkey, J.; Tata, A.; McKee, T. D.; Porcari, A. M.; Bluemke, E.; Woolman, M.; Ventura, M.; Eberlin, M. N.; Zarrine-Afsar, A., Variations in the Abundance of Lipid Biomarker Ions in Mass Spectrometry Images Correlate to Tissue Density. *Analytical Chemistry* **2016,** *88* (24), 12099-12107.
10. Mylonis, I.; Simos, G.; Paraskeva, E., Hypoxia-Inducible Factors and the Regulation of Lipid Metabolism. *Cells* **2019,** *8* (3).
11. Kamphorst, J. J.; Cross, J. R.; Fan, J.; de Stanchina, E.; Mathew, R.; White, E. P.; Thompson, C. B.; Rabinowitz, J. D., Hypoxic and Ras-transformed cells support growth by scavenging unsaturated fatty acids from lysophospholipids. *Proc Natl Acad Sci U S A* **2013,** *110* (22), 8882-7.
12. Bensaad, K.; Favaro, E.; Lewis, C. A.; Peck, B.; Lord, S.; Collins, J. M.; Pinnick, K. E.; Wigfield, S.; Buffa, F. M.; Li, J. L.; Zhang, Q.; Wakelam, M. J. O.; Karpe, F.; Schulze, A.; Harris, A. L., Fatty acid uptake and lipid storage induced by HIF-1alpha contribute to cell growth and survival after hypoxia-reoxygenation. *Cell Rep* **2014,** *9* (1), 349-365.
13. Ambrosio, M. R.; Di Serio, C.; Danza, G.; Rocca, B. J.; Ginori, A.; Prudovsky, I.; Marchionni, N.; del Vecchio, M. T.; Tarantini, F., Carbonic anhydrase IX is a marker of hypoxia and correlates with higher Gleason scores and ISUP grading in prostate cancer. *Diagn Pathol* **2016,** *11*.

14. Jiang, L.; Chughtai, K.; Purvine, S. O.; Bhujwalla, Z. M.; Raman, V.; Pasa-Tolic, L.; Heeren, R. M. A.; Glunde, K., MALDI-Mass Spectrometric Imaging Revealing Hypoxia-Driven Lipids and Proteins in a Breast Tumor Model. *Anal Chem* **2015,** *87* (12), 5947-5956.
15. Henderson, F.; Jones, E.; Denbigh, J.; Christie, L.; Chapman, R.; Hoyes, E.; Claude, E.; Williams, K. J.; Roncaroli, F.; McMahon, A., 3D DESI-MS lipid imaging in a xenograft model of glioblastoma: a proof of principle. *Sci Rep* **2020,** *10* (1), 16512.
16. Nielsen, M. M.; Lambertsen, K. L.; Clausen, B. H.; Meyer, M.; Bhandari, D. R.; Larsen, S. T.; Poulsen, S. S.; Spengler, B.; Janfelt, C.; Hansen, H. S., Mass spectrometry imaging of biomarker lipids for phagocytosis and signalling during focal cerebral ischaemia. *Sci Rep* **2016,** *6*, 39571.
17. Pettus, B. J.; Chalfant, C. E.; Hannun, Y. A., Ceramide in apoptosis: an overview and current perspectives. *Biochim Biophys Acta* **2002,** *1585* (2-3), 114-25.
18. Calligaris, D.; Norton, I.; Feldman, D. R.; Ide, J. L.; Dunn, I. F.; Eberlin, L. S.; Cooks, R. G.; Jolesz, F. A.; Golby, A. J.; Santagata, S.; Agar, N. Y., Mass spectrometry imaging as a tool for surgical decision-making. *J Mass Spectrom* **2013,** *48* (11), 1178-87.
19. Thomas, R. L., Jr.; Matsko, C. M.; Lotze, M. T.; Amoscato, A. A., Mass spectrometric identification of increased C16 ceramide levels during apoptosis. *J Biol Chem* **1999,** *274* (43), 30580-8.
20. Woolman, M.; Kuzan-Fischer, C. M.; Ferry, I.; Kiyota, T.; Luu, B.; Wu, M.; Munoz, D. G.; Das, S.; Aman, A.; Taylor, M. D.; Rutka, J. T.; Ginsberg, H. J.; Zarrine-Afsar, A., Picosecond infrared laser desorption mass spectrometry identifies medulloblastoma subgroups on intrasurgical timescales. *Cancer Res* **2019**.